

# High-Performance Sodium-Ion Pseudocapacitors Based on Hierarchically Porous Nanowire Composites

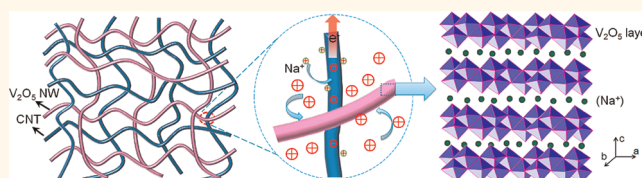
Zheng Chen,<sup>†</sup> Veronica Augustyn,<sup>‡</sup> Xilai Jia,<sup>†</sup> Qiangfeng Xiao,<sup>†</sup> Bruce Dunn,<sup>‡,\*</sup> and Yunfeng Lu<sup>†,\*</sup>

<sup>†</sup>Department of Chemical and Biomolecular Engineering and <sup>‡</sup>Department of Materials Science and Engineering, University of California, Los Angeles, California 90095, United States

Electrical energy storage plays an increasingly important role in modern society. In our daily lives, a number of portable devices, as well as the development of electric vehicles and smart grid energy storage, are highly dependent on lithium-ion energy storage devices. However, extensive use of such devices is likely to affect existing lithium reserves.<sup>1</sup> Seeking alternative materials for sustainable energy storage is emerging as an essential topic within the electrochemical energy storage community.

Sodium, the second lightest metallic element after lithium, is 4–5 orders of magnitude more abundant than lithium. In this context, it holds great promise for economical and sustainable energy storage devices. Moreover, the standard Na/Na<sup>+</sup> electrode potential (2.71 V) is very close to that of Li/Li<sup>+</sup> (3.02 V), and sodium-based non-aqueous electrolytes generally exhibit stabilities, ionic conductivities, and electrochemical windows comparable to their lithium-ion counterparts.<sup>2</sup> These features make sodium-ion-based electrochemical storage devices very attractive. A key requirement for Na-ion-based energy storage is finding suitable electrode materials in which to store sodium ions. Very recent studies show that sodium metal fluorophosphates,<sup>3</sup> lithium–sodium-mixed layered oxides,<sup>4</sup> and sodium manganese oxide<sup>5</sup> store impressive amounts of sodium and may serve as cathode materials for Na-ion batteries. For anode materials, some hard-carbon materials could show reasonable sodium storage capacities, but their cycling Li/ stability is poor.<sup>2,6</sup> Some nanocrystalline iron oxides may reversibly store Na<sup>+</sup> ions with capacities of 100–130 mAh g<sup>-1</sup>; however, their charge/discharge process is

## ABSTRACT



Electrical energy storage plays an increasingly important role in modern society. Current energy storage methods are highly dependent on lithium-ion energy storage devices, and the expanded use of these technologies is likely to affect existing lithium reserves. The abundance of sodium makes Na-ion-based devices very attractive as an alternative, sustainable energy storage system. However, electrodes based on transition-metal oxides often show slow kinetics and poor cycling stability, limiting their use as Na-ion-based energy storage devices. The present paper details a new direction for electrode architectures for Na-ion storage. Using a simple hydrothermal process, we synthesized interpenetrating porous networks consisting of layer-structured V<sub>2</sub>O<sub>5</sub> nanowires and carbon nanotubes (CNTs). This type of architecture provides facile sodium insertion/extraction and fast electron transfer, enabling the fabrication of high-performance Na-ion pseudocapacitors with an organic electrolyte. Hybrid asymmetric capacitors incorporating the V<sub>2</sub>O<sub>5</sub>/CNT nanowire composites as the anode operated at a maximum voltage of 2.8 V and delivered a maximum energy of ~40 Wh kg<sup>-1</sup>, which is comparable to Li-ion-based asymmetric capacitors. The availability of capacitive storage based on Na-ion systems is an attractive, cost-effective alternative to Li-ion systems.

**KEYWORDS:** nanocomposites · pseudocapacitors · V<sub>2</sub>O<sub>5</sub> nanowires · sodium-ion electrodes · high-rate

characterized by slow electrode kinetics.<sup>7</sup> To date, there is a lack of suitable anode materials for Na-ion batteries.

An alternative to energy storage with batteries is electrochemical capacitive storage, which offers faster charge and discharge operation, longer cycle life, and significantly higher power density than batteries.<sup>8,9</sup> Although most of this technology is based on carbon electrodes

\* Address correspondence to  
bdunn@ucla.edu,  
luucla@ucla.edu.

Received for review March 1, 2012  
and accepted April 3, 2012.

Published online April 04, 2012  
10.1021/nn300920e

© 2012 American Chemical Society

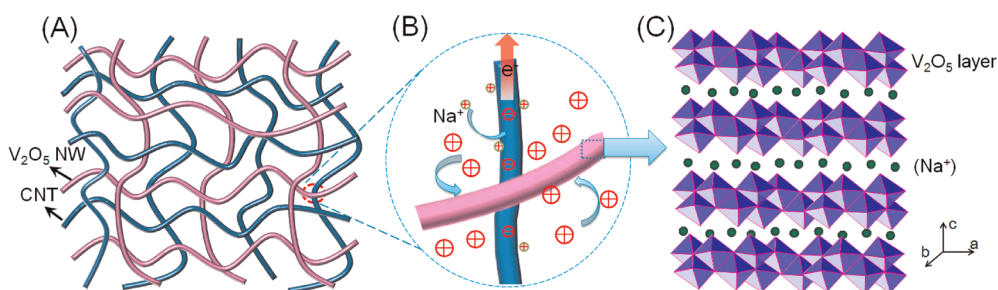


**Figure 1.** Schematic of (A) a nanocomposite consisting of interpenetrating networks of  $V_2O_5$  nanowires and CNTs, (B) intimate contacts between the  $V_2O_5$  nanowire and CNTs facilitating charge transport, and (C)  $Na^+$  intercalation within the  $V_2O_5$  layer structure.

which store energy *via* an electrical double layer, there recently has been considerable interest in using pseudocapacitance, which is based on faradaic reactions, to store energy.<sup>9,10</sup> The specific capacitance for pseudocapacitive materials can be an order of magnitude larger than that of carbon because of the higher levels of charge storage from redox reactions.<sup>9,11</sup> The most common devices which incorporate pseudocapacitive materials are hybrid asymmetric capacitors which typically have a carbon electrode as the cathode and the pseudocapacitor material as the anode.<sup>12,13</sup> Electrolytes can be aqueous or non-aqueous depending upon the pseudocapacitor material.<sup>9–13</sup>

In this work, we report a high-rate sodium-ion nanocomposite electrode material based on vanadium pentoxide ( $\alpha$ - $V_2O_5$ ) nanowires. These materials can be used as a pseudocapacitive anode for an asymmetric electrochemical capacitor.  $\alpha$ - $V_2O_5$  is a layered material that can accommodate a variety of metal ions, such as  $Li^+$ ,  $Na^+$ , and  $K^+$ ;<sup>14–17</sup> however, it generally exhibits poor electronic conductivity ( $\sigma \approx 10^{-6}$  to  $1 \Omega^{-1} \text{cm}^{-1}$ )<sup>16</sup> and slow ion diffusion. Recently, it was shown that electrodeposited  $V_2O_5$  thin-film electrodes can accommodate two  $Na/V_2O_5$ , achieving the theoretical capacity for sodium in vanadium oxide.<sup>18</sup> However, for device fabrication, thin films do not store adequate levels of energy, and for this reason, the electrode thickness should be at least in the micrometer range.<sup>19</sup> However, with such thicknesses, detrimental performance frequently occurs due to the increased electronic and ionic resistances. Fortunately, these technical barriers can be effectively circumvented by creating a porous composite architecture that integrates layer-structured  $V_2O_5$  nanowires with carbon nanotubes (CNTs). As illustrated in Figure 1, such a composite architecture consists of interpenetrating networks of  $V_2O_5$  nanowires and CNTs. The interpenetrating structure leads to the formation of interconnected pore channels which are filled by the electrolyte, thus ensuring facile ion transport and providing access of the electrolyte to the redox-active material. Furthermore, the conductive CNT network enables effective electron transport, while the small dimension of the nanowires shortens ion diffusion paths. As a result,

a fast pseudocapacitive charge storage process occurs, which seemingly avoids phase transformations during ion intercalation and deintercalation, and enables enhanced cycling stability. Because of the electronic conduction of the CNT, it is possible to increase the mass loading of the nanocomposite electrodes to as much as  $3 \text{ mg cm}^{-2}$ . At this loading density, asymmetric devices produce practical levels of energy and power, unlike submicrometer thick electrodes.<sup>19</sup> The high rate capability, capacity, and cycling stability of our Na-ion electrodes and asymmetric capacitors have not been achieved by other Na-ion materials. This work provides a promising direction for high-performance and sustainable energy storage systems.

## RESULTS AND DISCUSSION

Figure 2A shows a representative scanning electron microscope (SEM) image of a nanocomposite obtained directly from the *in situ* hydrothermal reaction, demonstrating nanowire  $V_2O_5$  networks penetrated with CNTs. The  $V_2O_5$  nanowires formed clusters due to the capillary force during water evaporation, while the CNTs are clearly observed penetrating through the nanowire network. Figure 2B shows a representative SEM image of the nanocomposite obtained from filtration and washing the as-synthesized product, which leads to the formation of a free-standing, flexible film (inset of Figure 2B). The nanocomposite, with 13 wt % of CNTs (determined from thermogravimetric analysis, Figure S1A in Supporting Information), demonstrates a continuous fibrous structure with abundant macropores formed by the network structure. A high-resolution SEM in Figure 2C shows a part of the composite film etched by 1% HF, indicating an intertwined porous network structure. The nanowires and CNTs possess an average diameter of  $\sim 50$  and  $\sim 30$  nm, respectively, and both of them have lengths of up to tens of micrometers. The formation of such interpenetrating networks relies on the dispersion of functionalized CNTs in solution followed by *in situ* growth of  $V_2O_5$  nanowires. The intertwined networks of the CNTs and nanowires exhibit an electrical conductivity of  $\sim 3.0 \text{ S cm}^{-1}$ , which is substantially higher than that of bulk  $V_2O_5$ .<sup>16,18</sup>

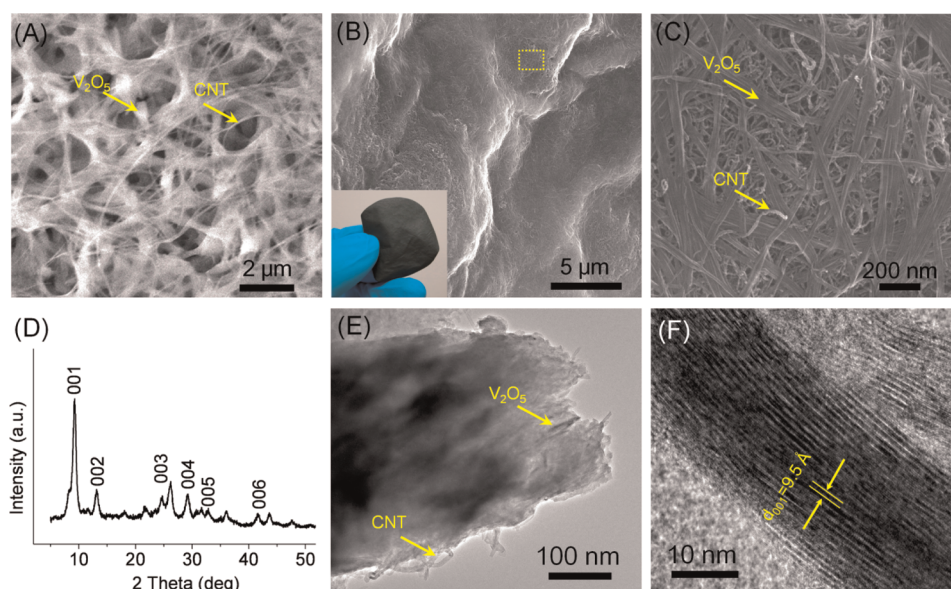
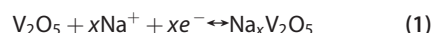


**Figure 2.** (A) SEM image of a  $V_2O_5$ /CNT nanocomposite demonstrating nanowire  $V_2O_5$  networks penetrated with CNTs. The sample was obtained directly from the as-synthesized product. While normal multi-walled CNTs were used for electrodes application, to better distinguish the individual  $V_2O_5$  and CNT from SEM image, super-long CNTs were chosen for this experiment.<sup>20</sup> (B) Representative low-magnification SEM image of a  $V_2O_5$ /CNT nanocomposite film obtained from filtration. Inset of panel B presents a digital photograph of such a flexible nanocomposite film. (C) High-magnification SEM image of the nanocomposites etched by 1 wt % HF. The image corresponds to the selected area in panel B. (D) XRD patterns of the nanocomposite showing typical 00 $l$  diffraction. (E) TEM image of a nanocomposite showing embedded CNTs within the  $V_2O_5$  nanowires. (F) HRTEM image of a  $V_2O_5$  nanowire showing the layered structure with  $d_{001}$  spacing of 0.95 nm.

Figure 2D shows a representative X-ray diffraction (XRD) pattern of the nanocomposite, suggesting a well-resolved layered structure with an interlayer spacing of  $\sim 1$  nm. The layered structure supports Na-ion transport, thus enabling the material to reversibly intercalate Na ions. The XRD pattern also suggests a small average crystallite grain size, which is calculated to be on the order of 9 nm using the Scherrer equation. The inappreciable diffraction peak of CNTs (at a  $2\theta$  of  $\sim 26^\circ$ , Figure S1B) is mainly due to the acid treatment of CNTs, which reduces the 002 ordering. In addition, the composite contains a relatively small mass fraction ( $\sim 13\%$ ) of CNTs. Figure 2E shows a transmission electron microscope (TEM) image of  $V_2O_5$  nanowires intertwined with CNTs. The nanowires and CNTs exhibit intimate interfaces due to the abundant hydrophilic groups ( $-\text{OH}$  and  $-\text{COOH}$ ) on their surfaces, which form a strong interaction upon drying. In addition, the high-resolution TEM (HRTEM) image shown in Figure 2F further suggests that the nanowires are composed of a layered crystalline structure with a layer-to-layer distance ( $d_{001}$ ) of  $\sim 9.5$  Å, in good agreement with XRD results. This structure is similar to the hydrothermally synthesized  $V_2O_5$  reported previously.<sup>20</sup> Besides the visible macroporous features observed from the microscopic images, nitrogen sorption isotherms (Figure S2A) suggest that such composites exhibit a hierarchically porous structure composed of abundant micropores ( $\sim 1.1$  nm) and mesopores (3–50 nm). The calculated average pore size is around 12 nm (assuming slit pore geometry), and

the porosity of the composite is  $\sim 58\%$ . Moreover, such nanocomposites exhibit a high BET (Brunauer–Emmett–Teller) surface area of around  $114 \text{ m}^2 \text{ g}^{-1}$ , which is substantially higher than bulk  $V_2O_5$  crystals ( $\sim 6 \text{ m}^2 \text{ g}^{-1}$ , Figure S2B). In short, the above physicochemical characterization indicates that the nanowire composite has a highly conductive, porous network structure with high surface area and hierarchical porosity, which are favorable features for fast electrode kinetics.

The electrochemical behavior of the nanocomposites was investigated using three-electrode cells with 1 M  $\text{NaClO}_4$  in propylene carbonate (PC) as an electrolyte, in which sodium foils were used as both the counter and reference electrodes. Charge storage behavior was characterized by cyclic voltammetry (CV). The electrochemical  $\text{Na}^+$  insertion/extraction process occurring at the  $V_2O_5$  electrodes can be represented by



where  $x$  is the mole fraction of inserted sodium ions.<sup>21</sup> Reversible charge storage is obtained by cycling the  $V_2O_5$ /CNT composite to 1.5 V, demonstrating that the structure is stable during  $\text{Na}^+$  insertion and extraction. Further charging of the electrode to lower potentials is possible, but the reaction might be less efficient due to irreversible structural changes.<sup>22–26</sup> A pure  $V_2O_5$  nanowire electrode (*i.e.*, without CNTs) shows appreciable capacity degradation during initial cycling ( $\sim 30\%$  capacity loss in the first 20 cycles), further confirming the advantage of utilizing  $V_2O_5$ /CNT nanocomposites for  $\text{Na}^+$  electrodes. It is worth mentioning that commercial

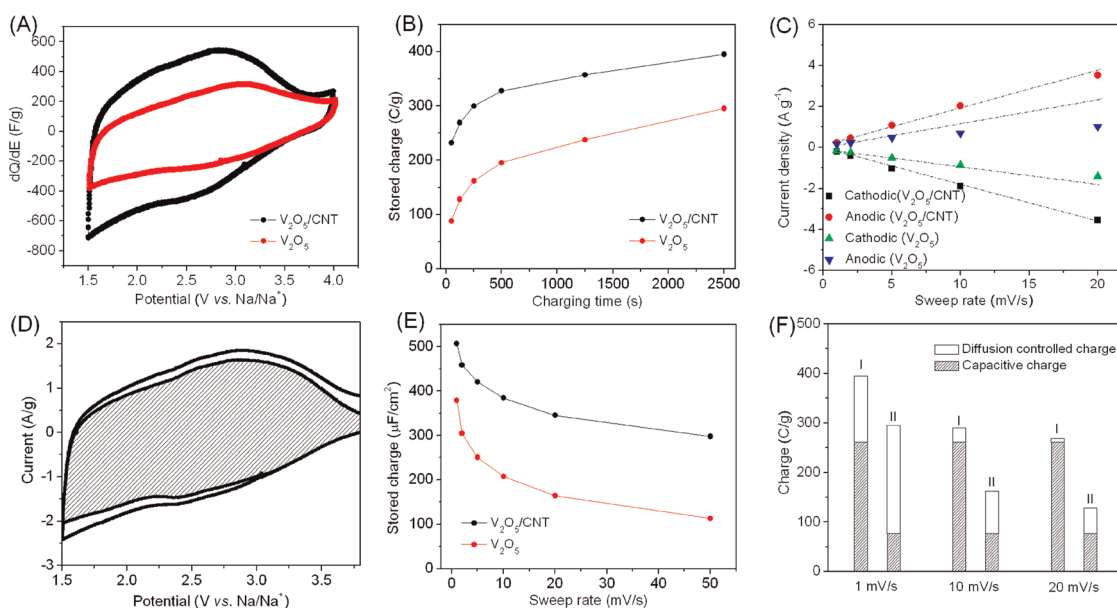


**Figure 3.** (A) Cyclic voltammograms (CVs) of  $V_2O_5/CNT$  and pure  $V_2O_5$  electrodes at a potential scan rate of  $2 \text{ mV s}^{-1}$  in  $1 \text{ M NaClO}_4$  in PC. The CV curves of the electrodes were acquired after 10–15 cycles in order to obtain stable capacities. (B) Kinetic behavior of  $V_2O_5/CNT$  and pure  $V_2O_5$  electrodes. (C) Voltammetric current (at  $2.5 \text{ V vs Na/Na}^+$ ) dependence on the sweep rate. (D) Capacitive and diffusion-controlled contribution to charge storage. The capacitive current is shaded and compared with the total measured current. (E) Surface-area normalized capacitance for  $V_2O_5/CNT$  and pure  $V_2O_5$  at different sweep rates. (F) Separation of contributions from capacitive and diffusion-controlled capacities at different sweep rates (I,  $V_2O_5/CNT$ ; II, pure  $V_2O_5$ ).

orthorhombic  $V_2O_5$  materials are not feasible for  $\text{Na}^+$  intercalation, possibly due to a rapid capacity degradation induced by structural changes (Figure S3).<sup>18</sup>

Figure 3A compares the cyclic voltammograms of a  $V_2O_5/CNT$  nanocomposite electrode and a pure  $V_2O_5$  nanowire electrode at a sweep rate of  $2 \text{ mV s}^{-1}$ . The nanocomposite electrode shows a pair of broad redox peaks between 2.4 and 2.8 V. The broad redox peaks arise from the large surface of the  $V_2O_5$  crystal structure and lead to numerous active sites over a wide range of energy levels.<sup>27–29</sup> Sodium-ion insertion/extraction into the  $V_2O_5/CNT$  nanocomposite occurs at similar potentials as lithium ions.<sup>30</sup> In contrast, the pure  $V_2O_5$  nanowire electrode shows an almost featureless CV curve due to the relatively poor kinetics arising from slow diffusion and inefficient electron transfer. Using the CV curves to calculate the specific capacitances of  $V_2O_5/CNT$  and pure  $V_2O_5$  electrodes (*vide infra*), we find that the nanocomposite electrode provides a capacity of  $\sim 400 \text{ C g}^{-1}$  between 1.5 and 3.5 V, which is higher than the  $V_2O_5$  electrode ( $\sim 300 \text{ C g}^{-1}$ ) and comparable to other high-performance Li-ion electrodes.<sup>27–30</sup>

To investigate the rate capability of the nanocomposite electrodes, CVs were carried out at different sweep rates, and the areas under the CV curves were used to determine the total electrode capacity.<sup>31</sup> Figure 3B compares the capacities of the nanocomposite and pure  $V_2O_5$  electrodes at sweep rates from 1 to  $50 \text{ mV s}^{-1}$  (Figure S4). For a typical voltage window at 1.5–4 V for  $V_2O_5$ -based electrodes, these rates correspond to a charge/discharge time between 50 and

2500 s. Without a CNT network, the pure  $V_2O_5$  nanowire electrode shows fast capacity degradation: the electrode loses  $\sim 70\%$  of its initial capacity as the charging time decreases from 2500 to 50 s. In contrast, the nanocomposite electrode exhibits a substantially higher capacity ( $\sim 400 \text{ C g}^{-1}$ ) at a charging time of 2500 s ( $1 \text{ mV s}^{-1}$ ) and still preserves 60% of the total capacity ( $\sim 240 \text{ C g}^{-1}$ ) as the charging time decreases to 50 s ( $50 \text{ mV s}^{-1}$ ). The substantial charge storage occurring on the order of a few minutes or less is a characteristic feature of capacitive storage. Such a high rate capability is consistent with the notion that the CNTs can effectively “wire” the small  $V_2O_5$  crystal domains and provide enhanced electronic conductivity, leading to an increased rate of charge transfer. While this behavior has been demonstrated with non-aqueous Li-ion electrolytes, the present work shows that comparable performance can be achieved with non-aqueous Na-ion electrolytes, thus making these materials of potential interest for high-rate sodium storage.<sup>30,32</sup>

In using CV to characterize the capacitive charge storage, one assumes that the current response is proportional to the sweep rate according to

$$i = dq/dt = C \times dE/dt = C \times v \quad (2)$$

where  $i$  is the current,  $q$  is the stored charge,  $C$  is the capacitance, and  $dE/dt$  is equal to the sweep rate  $v$ . Figure 3C shows the voltammetric current (*i.e.*, the current values at a potential of 2.5 V) dependence on the sweep rate (Figure S4). Note that the current response for the pure  $V_2O_5$  nanowire electrode

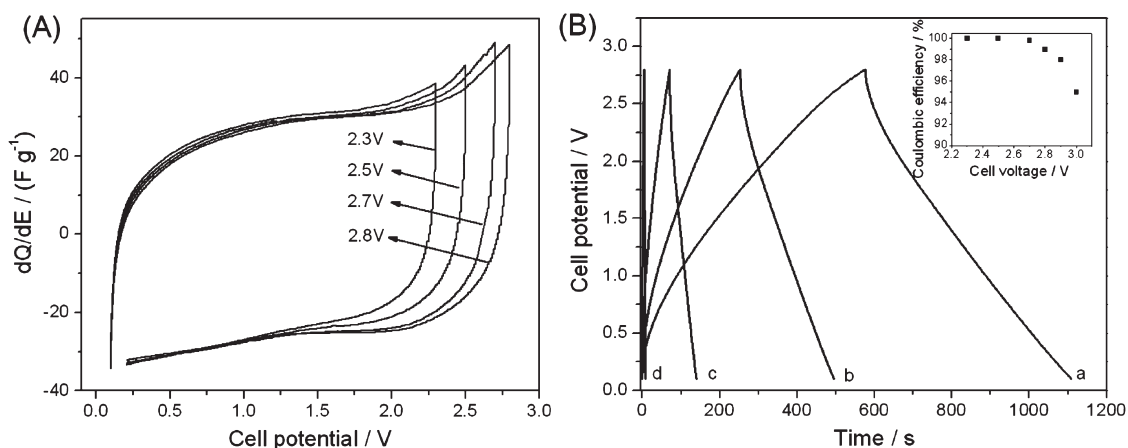


**Figure 4.** (A) CV curves of an asymmetric Na-ion supercapacitor device cycled in various potential windows at a sweep rate of  $2 \text{ mV s}^{-1}$ . (B) Galvanostatic charge/discharge curves from 0 to 2.8 V at different current densities in 1 M  $\text{NaClO}_4$  in PC (a, 0.5 mA; b, 1 mA; c, 3 mA; d, 15 mA; the footprint areas of anode and cathode were about 0.4 and  $1 \text{ cm}^2$ , respectively). Inset shows the dependence of Coulombic efficiency on the maximum charging voltage.

deviates from linearity as the sweep rate increases to  $10 \text{ mV s}^{-1}$ . This behavior is the result of slow charge transfer. This response was not observed for the  $\text{V}_2\text{O}_5/\text{CNT}$  electrode due to its better conductivity and hierarchical porosity. For both cathodic and anodic sweeps, a nearly perfect linear plot can be seen at sweep rates from 1 to  $20 \text{ mV s}^{-1}$ , confirming that the currents for the  $\text{V}_2\text{O}_5/\text{CNT}$  electrode are mainly capacitive in nature.

To quantitatively understand the charge storage mechanism for the nanocomposite electrode in the sodium-ion system, the measured current is separated into two components: (1) the capacitive contribution from pseudocapacitance and double-layer processes and (2) the contribution from diffusion-controlled current of  $\text{Na}^+$  insertion. Using the previous approach developed by Dunn *et al.*,<sup>29,33</sup> we were able to use the dependence of current on voltammetric sweep rate to quantitatively determine the capacitive contribution. Figure 3D shows the voltage profile at a sweep rate of  $10 \text{ mV s}^{-1}$  for the capacitive current (shaded region) in comparison to the total measured current. The capacitive contribution is 82% for the nanocomposite electrode, indicating that this is the dominant charge storage process. Since the surface areas of the nanocomposite and pure CNT are around 114 and  $210 \text{ m}^2 \text{ g}^{-1}$ , respectively, the surface-area normalized specific capacitance for  $\text{V}_2\text{O}_5$  in the composite is calculated to be approximately  $380 \mu\text{F cm}^{-2}$  at  $10 \text{ mV s}^{-1}$  (Figure 3E). This value is substantially higher than the pure  $\text{V}_2\text{O}_5$  electrode ( $205 \mu\text{F cm}^{-2}$ ) and about 1 order of magnitude higher than pure double-layer-based capacitances ( $5\text{--}20 \mu\text{F cm}^{-2}$ ).<sup>34–36</sup> This calculation confirms that charge storage of the  $\text{V}_2\text{O}_5/\text{CNT}$  nanocomposites in Na-ion electrolyte is primarily associated with pseudocapacitance. Our results also agree well with previous studies, which suggested that pseudocapacitive effects play an increasing role as the metal

oxide particle size decreases and/or the porosity increases.<sup>27–29,33,37</sup>

To further understand why such nanocomposites could store sodium ions with fast kinetics, we employed an analysis based on the work of Trasatti.<sup>38,39</sup> The total voltammetric charge ( $q_T$ ) of the electrode materials was separated into two parts: surface capacitive charge ( $q_s$ ) and diffusion-controlled charge ( $q_d$ ):

$$q_T = q_s + q_d \quad (3)$$

Due to its faster kinetics,  $q_s$  can be correlated with double-layer capacitance and pseudocapacitance, while  $q_d$  mainly depends on the slower diffusion process. Therefore, electrodes presenting a large fraction of  $q_s$  in the total capacity could exhibit a high rate capability. Assuming semi-infinite linear diffusion, within a reasonable range of sweep rates,  $q_s$  can be derived by plotting the total voltammetric charge  $q_T$  against the reciprocal of the square root of the potential sweep rate ( $\nu$ ) and extrapolating  $\nu$  to  $\infty$ , according to the following equation (Figure S5):

$$q_T = q_s + c\nu^{-1/2} \quad (4)$$

Deviation from the linearity of such a plot at high sweep rates is indicative of polarization effects that are ignored in the above equation.<sup>38,39</sup> The capacitive and diffusion-controlled contributions to total capacity are displayed in Figure 3F. It clearly shows that capacitive charge storage plays a significant role in the total capacity of the nanocomposite electrode, and that this role increases as the sweep rate increases. Thus, at  $1 \text{ mV s}^{-1}$ , capacitive processes account for some 70% of the charge storage, while at  $20 \text{ mV s}^{-1}$  it is 95%. This result is consistent with the capacitive current contribution shown in Figure 3C–E, strongly suggesting that most of the  $\text{V}_2\text{O}_5$  intercalation sites within the nanocomposites are easily accessible to the electrolyte. In contrast, the pure  $\text{V}_2\text{O}_5$  nanowire electrode has a

significant diffusion contribution to charge storage at all sweep rates, implying difficult ion access and charge transfer in the active material.

To assess the feasibility of using such nanocomposites for actual sodium-ion energy storage devices, we assembled coin-type asymmetric supercapacitors using the  $V_2O_5/CNT$  nanocomposite as an anode and a commercial activated carbon (with BET surface area of  $2100 \text{ m}^2 \text{ g}^{-1}$ , Figure S6) as a cathode material. Figure S7 shows a typical CV curve of the activated carbon (AC) electrode in the Na electrolyte, indicating a pure double-layer charge storage process. In such asymmetric devices, the charging process involves sodium insertion into the anode and perchlorate anion absorption onto the carbon cathode. Sodium extraction and perchlorate anion desorption occur on the anode and cathode, respectively, during a discharge process.<sup>12</sup> Due to the facile kinetics on both the anode and the cathode electrodes, this class of devices demonstrates high power and high energy density.

We evaluated the asymmetric supercapacitor using several techniques. On the basis of the storage capacities and electrochemical windows of both materials, an optimal mass ratio between the cathode and anode is found to be 3.8 in an asymmetric cell.<sup>13</sup> The devices show an open circuit potential of  $\sim 0.1 \text{ V}$ . Therefore, CV sweeps were performed from  $0.1 \text{ V}$  to different cell voltages to identify a suitable operating window. As shown in Figure 4A, the devices show rectangular CV curves at voltage windows up to  $2.8 \text{ V}$ , indicating an ideal capacitive behavior. However, further increasing the cell voltage caused appreciable irreversible capacitance, which should be avoided for long-term device operation. Galvanostatic cycling was also performed to evaluate the maximum voltage. Figure 4B (inset) shows the Coulombic efficiency ( $\eta$ ) of the prototypes at different maximum voltages. It is shown that devices operated over  $2.8 \text{ V}$  gave a Coulombic efficiency lower than 98%, probably due to irreversible reactions induced by overcharge. Therefore, the maximum cell voltage was controlled to  $2.8 \text{ V}$  for the device configuration.

Representative galvanostatic charge/discharge curves for the asymmetric prototypes at different current densities are shown in Figure 4B. At a charge/discharge time of  $\sim 18 \text{ min}$ , the devices provide an overall cell capacitance of  $\sim 35 \text{ F g}^{-1}$  (capacitance was calculated based on the total mass of cathode and anode active materials), giving an energy density of  $38 \text{ Wh kg}^{-1}$  and a power density of  $140 \text{ W kg}^{-1}$ . The energy density is close to that of lithium-ion asymmetric devices.<sup>30</sup> Even at a power density of  $\sim 5 \text{ kW kg}^{-1}$  (charge and discharge time of  $5.8 \text{ s}$ ), the devices still provide a cell capacitance of  $\sim 7 \text{ F g}^{-1}$ , corresponding to an energy density of  $\sim 7.5 \text{ Wh kg}^{-1}$ , an indication of the high power performance. From the internal resistance ( $iR$  drop) of the devices, a maximum power

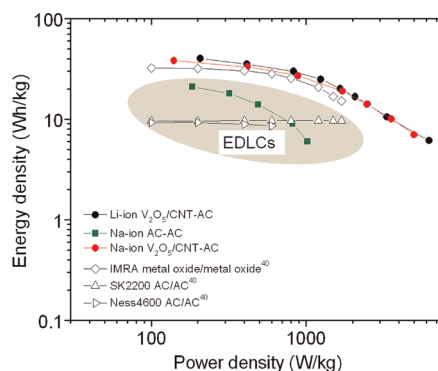


**Figure 5.** Ragone plots of Na-ion and Li-ion asymmetric supercapacitors made from a  $V_2O_5/CNT$  nanocomposite anode and an AC cathode, a symmetric supercapacitor made from the same AC, and various supercapacitor devices recently developed. All of the data are based on the mass of electrode materials. For the devices reported,<sup>40</sup> the mass of the electrode materials was estimated to be 40% of the total device weight. A packaging factor on the order of 0.4 was used.<sup>41–43</sup>

density was calculated to be  $45 \text{ kW kg}^{-1}$ . Moreover, the time constant ( $\tau = RC$ ) was calculated to be  $\sim 2.0 \text{ s}$ , which is comparable to conventional carbon-based supercapacitors ( $\sim 1 \text{ s}$ ), further confirming the high power capability.

For another perspective of the Na-ion asymmetric devices, Figure 5 compares the Ragone plots derived from galvanostatic cycling tests of different prototype supercapacitors. The power density is calculated based on the average power for each charge/discharge (Figure S8). Overall, the energy and power performance of the sodium-ion asymmetric supercapacitor is highly competitive with that of lithium-ion supercapacitors.<sup>30</sup> Moreover, these devices offer significantly higher energy and power than that of AC-based symmetric cells (Figure S9) and the current state-of-the-art electrical double-layer capacitor (EDLC) technology. Considering that the specific capacitance of the cathode materials (AC) is still relatively low (Figure S7), an even higher energy density could be realized if a better cathode material was available.

The sodium-ion devices based on the  $V_2O_5/CNT$  nanocomposites retained  $\sim 80\%$  of the initial capacity after 900 cycles at a charge/discharge rate of  $60 \text{ C}$  (power density of  $\sim 1700 \text{ W kg}^{-1}$ , Figure 6A). Electrochemical impedance spectroscopy (EIS) was used to determine whether any structural or interfacial changes occurred upon cycling the electrodes. Figure 6B shows the Nyquist plots for a sodium-ion asymmetric supercapacitor as a function of cycling. The cell exhibited similar uncompensated resistances ( $R_s$ ) from the electrolyte, current collectors, and contacts before and after cycling, indicating a stable electrode structure. A slight decrease of  $R_s$  was measured after the first cycle, which could be due to the *in situ* formation of a conductive sodium bronze ( $\text{Na}_x\text{V}_2\text{O}_5$ ).<sup>44</sup> The observed semicircles are

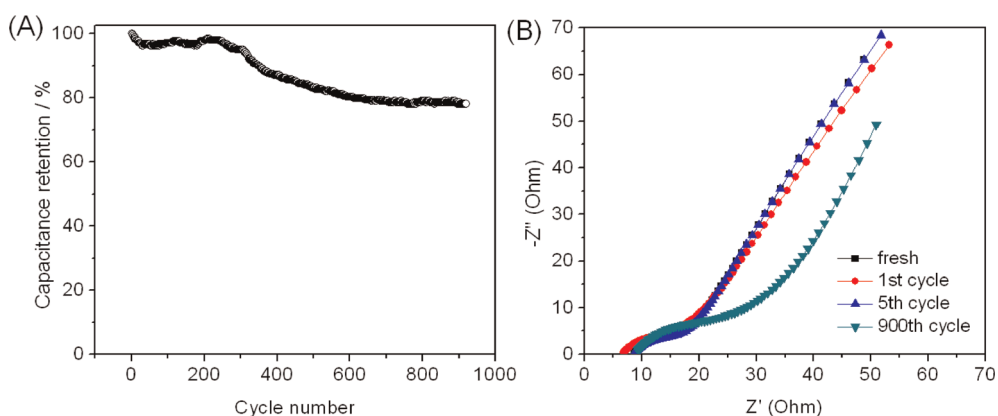


**Figure 6.** (A) Cycling performance of a  $V_2O_5$ /CNT-AC sodium-ion device for 900 cycles at a charge/discharge rate of 60 C. (B) Nyquist plots of the  $V_2O_5$ /CNT-AC hybrid sodium-ion device for different cycles (the plots of the fresh and 5th cycle electrode almost overlap).

caused by polarization or charge transfer resistance ( $R_c$ ) from both electrodes.<sup>45–48</sup> The  $R_c$  increased from  $\sim 10$  to  $\sim 20$  ohms after 900 cycles, which could be ascribed to an increased interfacial resistance due to interfacial changes or side reactions<sup>49</sup> occurring during the cycling process. The fact that  $R_c$  increased slowly in the first few cycles suggests that no obvious structure change occurred on the Na-ion electrode, and that a robust electrode structure can be maintained.<sup>50</sup> In addition, the decrease in cell capacitance on cycling may also be due to slight dissolution of the  $V_2O_5$  active material in the electrolyte.<sup>51</sup> The cycling results provide the insight that further improvements in cycling performance can be achieved by stabilizing the electrode interface and/or by judiciously choosing an electrolyte.

## CONCLUSIONS

In summary, we have demonstrated fast, reversible sodium-ion storage in  $V_2O_5$ /CNT nanocomposite electrodes. The  $V_2O_5$ /CNT nanocomposite exhibits far better rate capability and charge storage compared to  $V_2O_5$  electrodes that do not contain CNTs. Various analytical methods show that charge storage in these materials arises from a pseudocapacitive process. Using the nanocomposite electrode as an anode and commercial AC as a cathode, we have demonstrated that sodium-ion asymmetric capacitors in organic electrolyte exhibit excellent energy and power densities. These results show that sodium-ion-based energy storage devices can exhibit comparable performance to lithium-ion devices, thus providing an attractive, cost-effective alternative for a wide range of applications.

## METHODS

**Synthesis of the  $V_2O_5$ /CNT Nanocomposites.** The nanocomposites were synthesized through a one-pot hydrothermal process using aqueous vanadium oxide precursors in the presence of pretreated hydrophilic CNTs, which were synthesized by a mass production process with a capability of  $\sim 400$  tons year<sup>-1</sup>.<sup>52</sup> Grams of this composite were produced using a lab-scale reactor (volume of 120 mL). Details of the materials synthesis were described in previous publications.<sup>20,53</sup> The composition of the  $V_2O_5$ /CNT composite was determined by thermogravimetric analysis (TGA, Figure S1). Nitrogen sorption isotherms were measured at 77 K with a Micromeritics ASAP 2020. The specific surface areas were calculated by the Brunauer–Emmett–Teller (BET) method using an adsorption branch in a relative pressure range from 0.04 to 0.25. SEM and TEM experiments were conducted on a JEOL JSM-6700 FE-SEM and FEI Titan S/TEM operated at 300 kV, respectively.

**Electrochemical Characterization.** To make electrodes, the  $V_2O_5$ /CNT nanocomposites, pure  $V_2O_5$  nanowires, or activated carbon (AC) were assembled onto stainless steel current collectors. Briefly, 80% of the electrochemically active material, 10% carbon black, and 10% poly(vinylidene fluoride) (PVDF) dispersed in *N*-methylpyrrolidinone (NMP) were mixed to form slurries. The homogeneous slurries were coated on substrates

and dried at 90 °C for 30 min under vacuum. As-formed electrodes were then pressed at a pressure of 2 MPa and further dried for another 12 h. Typical mass loadings were 1–3 mg cm<sup>-2</sup> of active material on each current collector. The electrochemical measurements were carried out on a Bio-Logic VMP3 or Solartron 1860/1287. The electrolyte was 1 M NaClO<sub>4</sub> in propylene carbonate (PC) solution, and sodium foils were used as both the counter and reference electrodes. CV and EIS measurements were carried out in an argon-filled glovebox in three-electrode cells. To make 2032 type coin cells, glass fiber (GF/D) from Whatman was used as the separator. The cells were assembled under an argon atmosphere with moisture and oxygen levels of <1 ppm. In asymmetric devices, the operation windows for the nanocomposite anode and AC cathode are 1.5–3.2 and 3.3–4.3 V, respectively, and the maximum operation window of whole devices is 2.8 V.

The specific capacitance, power, and energy density were calculated based on the total masses of anode and cathode materials. The  $iR$  drop is used to calculate the cell's resistance using  $R = U/I$  and the RC constant by using  $\tau = R \times C_v$ , where  $C_v$  is the capacitance of the device and  $U$  is the maximum cell potential. The maximum power density is calculated based on  $P_{\max} = U^2/(4RM)$ .<sup>54</sup> The device energy density is calculated using  $E = 1/2CU^2$ , where  $C$  is the normalized cell capacitance.

Asymmetric cells were charged and discharged between 2.8 and 0.1 V, and AC-based symmetric cells were charged and discharged between 2.8 and 0 V. The charge stored by each electrode is determined by  $q = C_s m \Delta U$ , where  $C_s$  is the specific capacitance,  $\Delta U$  the potential range for the charge/discharge process, and  $m$  the mass of a single electrode. To obtain the maximum cell energy of the prototype supercapacitors, the cathode (represented by "ca") and anode (represented by "an") mass ratio was optimized according to  $m_{ca}/m_{an} = (C_{an}\Delta U_{an})/(C_{ca}\Delta U_{ca})$ . The total cell capacitance is calculated by  $C = I/[-(dU/dt)M]$ , where  $I$  is the discharge current density and  $M$  the total mass of anode and cathode materials.<sup>55</sup>

**Conflict of Interest:** The authors declare no competing financial interest.

**Acknowledgment.** This research work was supported as part of the Molecularly Engineered Energy Materials, an Energy Frontier Research Center funded by the U.S. Department of Energy, Office of Science, Office of Basic Energy Sciences under award DE-SC001342. V.A. was supported in part by the Office of Naval Research. The authors also acknowledge the support from General Motor Inc. and IMRA America Inc.

**Supporting Information Available:** Supplementary TGA, N<sub>2</sub> sorption isotherms, CV, galvanostatic charge/discharge data are included. This material is available free of charge via the Internet at <http://pubs.acs.org>.

## REFERENCES AND NOTES

- Tahil, W. *Meridian International Research*, 2007; [www.meridian-int-res.com](http://www.meridian-int-res.com).
- Stevens, D. A.; Dahn, J. R. High Capacity Anode Materials for Rechargeable Sodium-Ion Batteries. *J. Electrochem. Soc.* **2000**, *147*, 1271–1273.
- Ellis, B. L.; Makahnouk, W. R. M.; Makimura, Y.; Toghill, K.; Nazar, L. F. A Multifunctional 3.5 V Iron-Based Phosphate Cathode for Rechargeable Batteries. *Nat. Mater.* **2007**, *6*, 749–753.
- Kim, D.; Kang, S.-H.; Slater, M.; Rood, S.; Vaughey, J. T.; Karan, N.; Balasubramanian, M.; Johnson, C. S. Enabling Sodium Batteries Using Lithium-Substituted Sodium Layered Transition Metal Oxide Cathodes. *Adv. Energy Mater.* **2011**, *1*, 333–336.
- Cao, Y.; Xiao, L.; Wang, W.; Choi, D.; Nie, Z.; Yu, J.; Saraf, L. V.; Yang, Z.; Liu, J. Reversible Sodium Ion Insertion in Single Crystalline Manganese Oxide Nanowires with Long Cycle Life. *Adv. Mater.* **2011**, *23*, 3155–3160.
- Wenzel, S.; Hara, T.; Janek, J.; Adelhelm, P. Room-Temperature Sodium-Ion Batteries: Improving the Rate Capability of Carbon Anode Materials by Templating Strategies. *Energy Environ. Sci.* **2011**, *4*, 3342–3345.
- Komaba, S.; Mikumo, T.; Yabuuchi, N.; Ogata, A.; Yoshida, H.; Yamada, Y. Electrochemical Insertion of Li and Na Ions into Nanocrystalline Fe<sub>3</sub>O<sub>4</sub> and  $\alpha$ -Fe<sub>2</sub>O<sub>3</sub> for Rechargeable Batteries. *J. Electrochem. Soc.* **2010**, *157*, A60–A65.
- Miller, J. R.; Simon, P. Electrochemical Capacitors for Energy Management. *Science* **2008**, *321*, 651–652.
- Simon, P.; Gogotsi, Y. Materials for Electrochemical Capacitors. *Nat. Mater.* **2008**, *7*, 845–854.
- Zhang, L. L.; Zhao, X. S. Carbon-Based Materials as Supercapacitor Electrodes. *Chem. Soc. Rev.* **2009**, *38*, 2520–2531.
- Conway, B. E.; Birss, V.; Wojtowicz, J. The Role and Utilization of Pseudocapacitance for Energy Storage by Supercapacitors. *J. Power Sources* **1997**, *66*, 1–14.
- Amatucci, G. G.; Badway, F.; Pasquier, A. D.; Zheng, T. An Asymmetric Hybrid Nonaqueous Energy Storage Cell. *J. Electrochem. Soc.* **2001**, *148*, A930–A939.
- Khomenko, V.; Raymundo-Piñero, E.; Béguin, F. Optimization of an Asymmetric Manganese Oxide/Activated Carbon Capacitor Working at 2 V in Aqueous Medium. *J. Power Sources* **2006**, *153*, 183–190.
- Tang, P. E.; Sakamoto, J. S.; Baudrin, E.; Dunn, B. V<sub>2</sub>O<sub>5</sub> Aerogel as a Versatile Host for Metal Ions. *J. Non-Cryst. Solids* **2004**, *350*, 67–72.
- Livage, J. Vanadium Pentoxide Gels. *Chem. Mater.* **1991**, *3*, 578–593.
- Badot, J. C.; Baffier, N. Ionic Conductivity and Dielectric Properties of Vanadium Pentoxide Xerogels. *J. Mater. Chem.* **1992**, *2*, 1167–1175.
- Whittingham, M. S.; Song, Y.; Lutta, S.; Zavalij, P. Y.; Chernova, N. A. Some Transition Metal (Oxy)phosphates and Vanadium Oxides for Lithium Batteries. *J. Mater. Chem.* **2005**, *15*, 3362–3379.
- Tepavcevic, S.; Xiong, H.; Stamenkovic, V. R.; Zuo, X.; Balasubramanian, M.; Prakapenka, V. B.; Johnson, C. S.; Rajh, T. Nanostructured Bilayered Vanadium Oxide Electrodes for Rechargeable Sodium-Ion Batteries. *ACS Nano* **2012**, *6*, 530–538.
- Gogotsi, Y.; Simon, P. True Performance Metrics in Electrochemical Energy Storage. *Science* **2011**, *334*, 917–918.
- Jia, X.; Chen, Z.; Suwarnasarn, A.; Rice, L.; Wang, X.; Sohn, H.; Zhang, Q.; Wu, M. B.; Wei, F.; Lu, Y. High-Performance Flexible Lithium-Ion Electrodes Based on Robust Network Architecture. *Energy Environ. Sci.* **2012**, DOI: 10.1039/C2EE03110H.
- Su, L.; Winnick, J.; Kohl, P. Sodium Insertion into Vanadium Pentoxide in Methanesulfonyl Chloride-Aluminum Chloride Ionic Liquid. *J. Power Sources* **2001**, *101*, 226–230.
- Coustier, F.; Hill, J.; Owens, B. B.; Passerini, S.; Smyrl, W. H. Doped Vanadium Oxides as Host Materials for Lithium Intercalation. *J. Electrochem. Soc.* **1999**, *146*, 1355–1360.
- Leger, C.; Bach, S.; Soudan, P.; Pereira-Ramos, J. P. Structural and Electrochemical Properties of  $\omega$ -Li<sub>x</sub>V<sub>2</sub>O<sub>5</sub> (0.4 < x < 3) as Rechargeable Cathodic Material for Lithium Batteries. *J. Electrochem. Soc.* **2005**, *152*, A236–A241.
- Zhan, S. Y.; Wang, C. Z.; Nikolowski, K.; Ehrenberg, H.; Chen, G.; Wei, Y. J. Electrochemical Properties of Cr Doped V<sub>2</sub>O<sub>5</sub> between 3.8 and 2.0 V. *Solid State Ionics* **2009**, *180*, 1198–1203.
- Hu, Y.-S.; Liu, X.; Müller, J.-O.; Schlögl, R.; Maier, J.; Su, D. S. Synthesis and Electrode Performance of Nanostructured V<sub>2</sub>O<sub>5</sub> by Using a Carbon Tube-in-Tube as a Nanoreactor and an Efficient Mixed-Conducting Network. *Angew. Chem., Int. Ed.* **2009**, *48*, 210–214.
- Mai, L.; Xu, L.; Han, C.; Xu, X.; Luo, Y.; Zhao, S.; Zhao, Y. Electrospun Ultralong Hierarchical Vanadium Oxide Nanowires with High Performance for Lithium Ion Batteries. *Nano Lett.* **2010**, *10*, 4750–4755.
- Swider-Lyons, K. E.; Love, C. T.; Rolison, D. R. Improved Lithium Capacity of Defective V<sub>2</sub>O<sub>5</sub> Materials. *Solid State Ionics* **2002**, *152–153*, 99–104.
- Brezesinski, T.; Wang, J.; Polleux, J.; Dunn, B.; Tolbert, S. H. Templated Nanocrystal-Based Porous TiO<sub>2</sub> Films for Next-Generation Electrochemical Capacitors. *J. Am. Chem. Soc.* **2009**, *131*, 1802–1809.
- Brezesinski, T.; Wang, J.; Tolbert, S. H.; Dunn, B. Ordered Mesoporous  $\alpha$ -MoO<sub>3</sub> with Iso-oriented Nanocrystalline Walls for Thin-Film Pseudocapacitors. *Nat. Mater.* **2010**, *9*, 146–151.
- Chen, Z.; Augustyn, V.; Wen, J.; Zhang, Y.; Shen, M.; Dunn, B.; Lu, Y. High-Performance Supercapacitors Based on Intertwined CNT/V<sub>2</sub>O<sub>5</sub> Nanowire Nanocomposites. *Adv. Mater.* **2011**, *23*, 791–795.
- Pang, S.-C.; Anderson, M. A.; Chapman, T. W. Novel Electrode Materials for Thin-Film Ultracapacitors: Comparison of Electrochemical Properties of Sol–Gel-Derived and Electrodeposited Manganese Dioxide. *J. Electrochem. Soc.* **2000**, *147*, 444–450.
- Kim, I.-H.; Kim, J.-H.; Cho, B.-W.; Lee, Y.-H.; Kim, K.-B. Synthesis and Electrochemical Characterization of Vanadium Oxide on Carbon Nanotube Film Substrate for Pseudocapacitor Applications. *J. Electrochem. Soc.* **2006**, *153*, A989–A996.
- Wang, J.; Polleux, J.; Lim, J.; Dunn, B. Pseudocapacitive Contributions to Electrochemical Energy Storage in TiO<sub>2</sub> (Anatase) Nanoparticles. *J. Phys. Chem. C* **2007**, *111*, 14925–14931.

34. Frackowiak, E. Carbon Materials for Supercapacitor Application. *Phys. Chem. Chem. Phys.* **2007**, *9*, 1774–1785.
35. Barbieri, O.; Hahn, M.; Herzog, A.; Kötz, R. Capacitance Limits of High Surface Area Activated Carbons for Double Layer Capacitors. *Carbon* **2005**, *43*, 1303–1310.
36. Chmiola, J.; Yushin, G.; Gogotsi, Y.; Portet, C.; Simon, P.; Taberna, P. L. Anomalous Increase in Carbon Capacitance at Pore Sizes Less Than 1 Nanometer. *Science* **2006**, *313*, 1760–1763.
37. Balaya, P.; Bhattacharyya, A.; Jamnik, J. J.; Zhukovskii, Y. F.; Kotomin, E. A.; Maier, J. Nano-ionics in the Context of Lithium Batteries. *J. Power Sources* **2006**, *159*, 171–178.
38. Ardizzone, S.; Fregonara, G.; Trasatti, S. "Inner" and "Outer" Active Surface of RuO<sub>2</sub> Electrodes. *Electrochim. Acta* **1990**, *35*, 263–267.
39. Baronetto, D.; Krstajic, N.; Trasatti, S. Reply to "Note on a Method to Interrelate Inner and Outer Electrode Areas" by H. Vogt. *Electrochim. Acta* **1994**, *39*, 2359–2362.
40. Burke, A. F. The Present and Projected Performance and Cost of Double-layer and Pseudo-capacitive Ultracapacitors for Hybrid Vehicle Applications. Proc. IEEE Veh. Power Propulsion Conf. (VPPC'05), **2005**, 356–366.
41. Lee, S. W.; Yabuuchi, N.; Gallant, B. M.; Chen, S.; Kim, B. S.; Hammond, P. T.; Shao-Horn, Y. High-Power Lithium Batteries from Functionalized Carbon-Nanotube Electrodes. *Nat. Nanotechnol.* **2010**, *5*, 531–537.
42. Eaves, S.; Eaves, J. A Cost Comparison of Fuel-Cell and Battery Electric Vehicle. *J. Power Sources* **2004**, *130*, 208–212.
43. Appetecchi, G. B.; Prosini, P. P. 0.4 Ah Class Graphite/LiMn<sub>2</sub>O<sub>4</sub> Lithium-Ion Battery Prototypes. *J. Power Sources* **2005**, *146*, 793–797.
44. Bach, S.; Baffier, N.; Pereira-Ramos, J. P.; Messina, R. Electrochemical Sodium Intercalation in Na<sub>0.33</sub>V<sub>2</sub>O<sub>5</sub> Bronze Synthesized by a Sol–Gel Process. *Solid State Ionics* **1989**, *37*, 41–49.
45. Fischer, A. E.; Pettigrew, K. A.; Rolison, D. R.; Stroud, R. M.; Long, J. W. Incorporation of Homogeneous, Nanoscale MnO<sub>2</sub> within Ultraporos Carbon Structures via Self-Limiting Electroless Deposition: Implications for Electrochemical Capacitors. *Nano Lett.* **2007**, *7*, 281–286.
46. Shaju, K. M.; Bruce, P. G. A Stoichiometric Nano-LiMn<sub>2</sub>O<sub>4</sub> Spinel Electrode Exhibiting High Power and Stable Cycling. *Chem. Mater.* **2008**, *20*, 5557–5562.
47. Ma, H.; Zhang, S.; Ji, W.; Tao, Z.; Chen, J.  $\alpha$ -CuV<sub>2</sub>O<sub>6</sub> Nanowires: Hydrothermal Synthesis and Primary Lithium Battery Application. *J. Am. Chem. Soc.* **2008**, *130*, 5361–5367.
48. Brezesinski, T.; Wang, J.; Senter, R.; Brezesinski, K.; Dunn, B.; Tolbert, S. H. On the Correlation between Mechanical Flexibility, Nanoscale Structure, and Charge Storage in Periodic Mesoporous CeO<sub>2</sub> Thin Films. *ACS Nano* **2010**, *4*, 967–977.
49. Kim, J. W.; Augustyn, V.; Dunn, B. The Effect of Crystallinity on the Rapid Pseudocapacitive Response of Nb<sub>2</sub>O<sub>5</sub>. *Adv. Energy Mater.* **2012**, *2*, 141–148.
50. Naoi, K. "Nanohybrid Capacitor": The Next Generation Electrochemical Capacitors. *Fuel Cells* **2010**, *5*, 825–833.
51. Sudant, G.; Baudrin, E.; Dunn, B.; Tarascon, J.-M. Synthesis and Electrochemical Properties of Vanadium Oxide Aergels Prepared by a Freeze-Drying Process. *J. Electrochem. Soc.* **2004**, *151*, A666–A671.
52. Wei, F.; Zhang, Q.; Qian, W. Z.; Yu, H.; Wang, Y.; Luo, G. H.; Xu, G. H.; Wang, D. Z. The Mass Production of Carbon Nanotubes Using a Nano-Agglomerate Fluidized Bed Reactor: A Multiscale Space-Time Analysis. *Powder Technol.* **2008**, *183*, 10–20.
53. Chen, Z.; Qin, Y.; Weng, D.; Xiao, Q.; Peng, Y.; Wang, X.; Li, H.; Wei, F.; Lu, Y. Design and Synthesis of Hierarchical Nanowire Composites for Electrochemical Energy Storage. *Adv. Funct. Mater.* **2009**, *19*, 3420–3426.
54. Burke, A. Ultracapacitors: Why, How, and Where Is the Technology. *J. Power Sources* **2000**, *91*, 37–50.
55. Brousse, T.; Toupin, M.; Bélanger, D. A Hybrid Activated Carbon-Manganese Dioxide Capacitor Using a Mild Aqueous Electrolyte. *J. Electrochem. Soc.* **2004**, *151*, A614–A622.